4

Laser welding of aluminium-steel clad materials for naval applications

Roberto Spina and Luigi Tricarico
Dept. of Mechanical & Management Engineering - Politecnico di Bari
Italy

1. Introduction

Several electronic, naval, aeronautic and automotive components are made by different materials joined together in order to improve mechanical and functional properties. Functionalities provided by clad metals can be grouped into structural, thermal expansion management, thermo-mechanical control, electrical, magnetic, corrosion resistant, joining and cosmetic applications to cite as few (*Chen et al., 2005*). The demand for dissimilar material joints continuously grows because one material can provide only a small spectrum of chemical, physical and mechanical characteristics required for the investigated application respect to the bi- or multi-layer material joints. Moreover considerable weight savings can be achieved by using lightweight materials clad to strength ones directly. For these reasons, researchers and manufacturers continuously evaluate the application of traditional and/or advanced joining processes to clad dissimilar materials and obtain transition joints optimally. Focusing the attention on steel/aluminium joints and shipbuilding industry, the development of lightweight and fast-speed vessels requires a great number of aluminium/steel structural transition joints (STJs) in order to connect aluminium superstructures to the steel hull (*Chao et al., 1997*). Using this solution, the total weight of a ship is reduced due to the lighter aluminium superstructure. However, problems in service may occurred by relations at the atomic level between iron and aluminium and differences existing in physical and chemical properties of the base metals. One of the most undesired effect derives from the large electrochemical difference of 1.22 volts between iron and aluminium that causes a high susceptibility to both inter-crystalline and galvanic corrosion along the STJ interface.
Fusion welding processes, initially used to produce the aluminium/steel STJs with desired physical and mechanical features, are narrowly applied because the subsidiary precipitates and brittle Al/Fe inter-metallic phases, created during fusion and solidification and located along the interface, are severely exposed to corrosion, troubling joint cohesion (*Durgutlu et al., 2005*). The high heat input affects the different thermal properties of the two materials—thermal expansion, heat capacity and thermal conductivity—and may lead to very complex stress fields. Moreover, the heat input causes the lattice transformation and the formation of inter-metallic phases. In iron (cubic body-centred up to 911 °C) and aluminium (cubic face-centred) joints, the inter-metallic phases present a high hardness and low ductility. The

welding procedures of STJs must be carefully controlled in order to avoid disbonding during construction and/or failure during service. The thickness of the Al/Fe inter-metallic layer between parent materials plays an important role in obtaining joints with optimum performances. Thus, the thickness minimisation of Al/Fe inter-metallic phases represents one of the most important problems to solve. This is why all the heat-intensive processes used up until now have been designed to keep the formation of inter-metallic phases within tight limits or even to prevent them from occurring in the first place (*Bruckner, 2003; Chen & Kovacevic, 2004*).
Solid-state processes seems to be more likely for producing STJs because thin inter-metallic thicknesses are achieved. Processes normally employed are roll bonding, pressure welding, friction welding, ultrasonic welding, diffusion bonding and explosive welding (*Deqing et al., 2007*). Explosion-welding is a fast and efficient process to bond two or more different metals with satisfactory corrosive properties. The energy of an explosive detonation is used to create a metallurgical weld between dissimilar materials. In preparation, the cladding plate is placed over the backer plate with a small gap between the two, ground and fixtured parallel at a precise spacing. A measured quantity of a specifically formulated explosive is spread on top of the cladding plate. On detonation, the cladding plate collides progressively with the backer plate at a high velocity. This collision removes the contaminating surface films like oxides and absorbed gases in the form of a fine jet, bringing together two virgin metal surfaces to form a metallurgical bond by electron sharing. The detonation front then uniformly travels across the surface until the end of the plates (*Durgutlu et al., 2005; Bankers & Nobili, 2002*). The combination of surface cleaning and extreme pressure produces a continuous metallurgical weld (*Young & Banker, 2004*). Although the explosion generates intense heat, there is no sufficient time for the heat to conduct into the metals, avoiding bulk heating (*ASM Handbook Vol.6*). Furthermore, there are no changes in the metallurgical characteristics or specification compliance of the component metals.
The objective of the present research is the evaluation of the process feasibility of applying laser welding to explosion-bonded STJs for the final ship assembly. This paper reports results achieved for as-simulated laser welded conditions by imposing severe thermal cycles to specimen obtained from structural transition joints with time periods longer than those normally recorded during laser welding. Metallurgical and mechanical characterisation of heat treated specimen are performed to evaluate the influence of the heat treatments on final joint properties. The analysis was then extended to the bead on plate and double side/double square fillet T-joints.

2. Problem Position

From the chemical point of view, iron reacts with aluminium forming several Fe_xAl_y inter-metallic compounds, as the Fe-Al phase diagram shows (Figure 1).
Only small amounts of iron can be dissolved in aluminium and only small amounts of aluminium can be dissolved in iron. The $FeAl_2$, Fe_2Al_5, Fe_2Al_7 and $FeAl_3$ are Al-rich inter-metallic compounds while FeAl and Fe_3Al are Fe-rich inter-metallic compounds (Table 1). The presence of Al-rich inter-metallic phases must be accurately control to reduce their influence on joint performances, respect to the Fe-rich phases with higher toughness values. In fact the complex lattice structures and too high micro-hardness values (up to 800 HV or more) of Al-rich inter-metallic compounds can cause a high interface fragility.

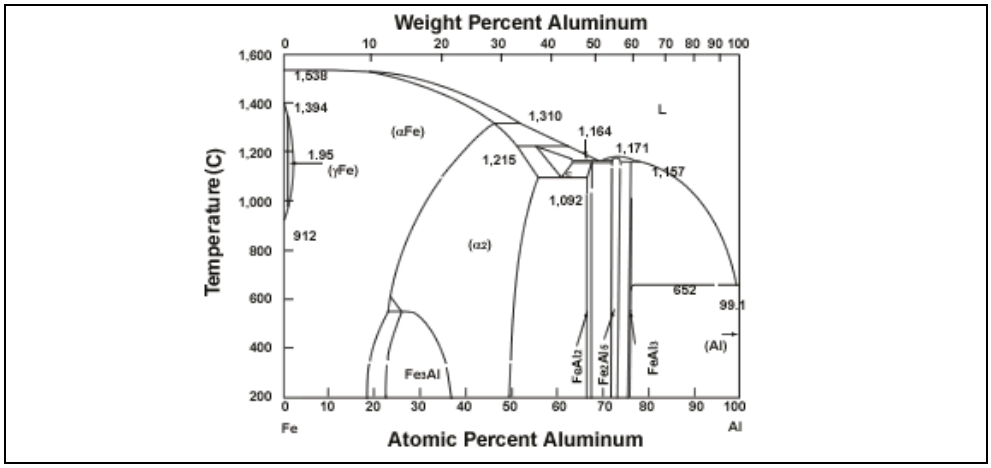

Fig. 1. Fe-Al phase diagram at equilibrium.

Phase	Al Content (atomic %)	Structure	Micro-hardness (HV)	Density (g/cm³)
Fe_3Al	25	Ordered BCC	250-350	6.67
FeAl	50	Ordered BCC	400-520	5.37
Fe_2Al_7	63	Complex BCC	650-680	NA
$FeAl_2$	66-67	Complex rhombohedral	1,000-1,050	4.36
Fe_2Al_5	69.7-73.2	BCC orthorhombic	1,000-1,100	4.11
$FeAl_3$	74-76	Highly complex monoclinic BCC	820-980	3.95

Table 1. Inter-metallic compounds (*Bruckner, 2003*).

The inter-metallic phases occurs at temperatures below the melting point of aluminium not only during explosion welding but also during fusion welding necessary to connect STJs to the steel hull and aluminium superstructure. The formation rate of the inter-metallic phases is diffusion-driven, thus dependent from time and temperature variables. For this reason, the evaluation of joint characteristics before and after fusion welding is necessary. The mechanical and metallurgical properties of the bond zone are determined by means of tests made in the following conditions (*American Bureau of Shipping, 2000*):

- As-clad condition: No preliminary treatment is given to the specimens to represent the as-clad product.
- As-simulated welded condition: A preliminary heat treatment is performed to the specimens in order to represent the product after welding.

The simulated welded specimens are heat-treated at 315±14°C (600F±25 °F) for 15 minutes, as suggested by American Bureau of Shipping. This temperature-time limit is settled-on by considering that a STJ exposed to a higher time or higher temperature than this limit can present a lower performance life than any as-clad explosion-welded STJs. However, two main considerations have to be made on this temperature-time limit such as: (i) the interaction between the temperature and time variables is not accurately evaluated and (ii) the welded condition normally is refereed to TIG or MIG welding processes, both characterised by high heat input profiles. The main hypothesis to verify is whether a very

short time at a high temperature may sufficient to compromise and, in the worst condition, destroy bond properties of explosion-welding STJs, making the application of laser welding unfeasible. All above considerations shift the manufacturing problem form suppliers to shipbuilders. In fact, the interest of an STJ is its direct application instead of the way it is produced.

3. Specimen preparation of heat treatment

A tri-metallic transition joint was chosen for this study due to its industrial importance for the fast vessel construction. The rough material was the Triclad® STJ, a trade name of Merrem & la Porte for aluminium/steel transition joints, produced with open-air explosion welding. In particular, the selected rough material consisted of an ASTM A516 steel backer plate clad to an AA5083 flyer plate, with commercial purity aluminium (AA1050) interlayer plate placed between the former two. The presence of the AA1050 interlayer was necessary to improve STJ diffusion resistance with both iron and aluminium (*Bankers & Nobili, 2002*). The investigated STJ, realised by the supplier in compliance with specification ASTM B898 (*Chen et al., 2005*), was analysed with ultrasonic inspection from the manufacturer to confirm the whole weld interface integrity.

STJ specimens for metallographic and micro-hardness evaluation of about 28·13·3 mm^3 (Figure 2) were sectioned by using an abrasive wheel cut-off machine in transverse direction to the length of the rough plate, taking care of minimising the mechanical and thermal distortions of the Al/Fe interface. The specimen surfaces were smoothly ground to give a uniform finish and cleaned before putting them in the heat treatment oven. Each specimen was heated at specific temperature and time in compliance with the Central Composite Design (CCD) experimental plan and cooled outside the heat oven to the room temperature. The CCD design is a factorial or fractional factorial design (with centre points) in which "star" points are added to estimate curvature (*Montgomery, 2000*). The main CCD factors were the temperature and time, ranging between 100 and 500°C and 5 and 25 minutes respectively. The centre point of the CCD, replicated five times, was fixed at 300°C for 15 minutes, according to the limit of the as-simulated welded condition. The entire plan, shown in Table 2, also included the as-clad condition (ID 12) and near-melted condition of aluminium alloys (ID 13). The temperature of the heat treatment oven was rapidly reached by applying a high heat power and then maintaining this temperature for time sufficient to guarantee stationary conditions. The specimen was then inserted into the oven. This process was repeated for all specimens.

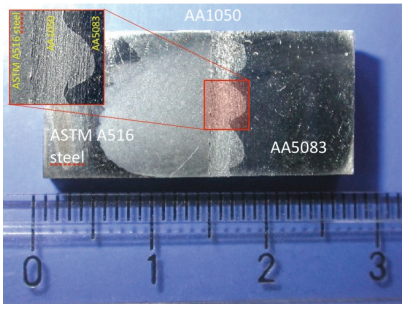

Fig. 2. Triclad® STJ.

Specimen ID	Temperature (°C)	Time (minutes)
1	100	5
2	100	25
3	500	5
4	500	25
5-6-7-8-9	300	15
10	300	0.86
11	300	29.14
12	17.16	15
13	582.4	15

Table 2. Central Composite DOE.

The heat-treated specimens were then prepared by grinding with 200 to 1000-grit silicon carbide papers, followed by mechanical polishing from 6-µm to 1-µm diamond abrasive on short nap clothes. Etching was then performed on the steel side of specimens with Nital solution (2 mL HNO_3 and 98 mL of C_2H_5OH) in distilled water for 15 seconds in order to highlight grain structures as well as inter-metallic phases. Keller's reagent (5 mL HNO_3 and 190 mL of H_2O) was applied for 15 seconds to aluminium side to point macro-structures.

4. Metallographic examination of heat treated specimens

The visual inspection of the STJ specimens by using the metallographic microscope was very useful to investigate modifications of Al/Fe interface due to heat treatments. The as-clad specimen was initially analysed and different areas were detected, as Figure 3 shows. Ripples with different morphological characteristics were located at the interface. These ripples, formed from the rapid quenching of melt regions caused by explosion, consisted of a mixture of different inter-metallic phases, as the grey scale variation suggests (Figure 3-A/B). Areas surrounding these ripples, and sometimes located inside them, exhibited the typical dendrite morphology of a slow cooling process after melting . Small-sized clusters of inter-metallic compounds, formed in not equilibrium cooling conditions, were also observed along the Al/Fe interface, pointing out the interface discontinuity. The cluster thickness ranged between 50 and 160 µm. Along the Al/Fe interface, the inter-metallic phases were detected as a discontinuous narrow band, less than 5 µm wide (Figure 3-C/D). This band was thick in areas submitted to high thermal gradient while it was very thin or absent in areas subjected to very low thermal gradient. The very brittle inter-metallic phases identified in this band at room temperature in the as-clad STJ were the $FeAl_3$ and Fe_2Al_5 on the aluminium side and steel side respectively, as confirmed by quantitative analysis (x-ray diffraction) performed with SEM (Figure 4). Further metallographic features were noted for the STJ base materials. The micro-structure of the ASTM A516 steel consisted of ferrite (lighter constituent) with pearlite (darker constituent), as Figure 3-E shows. Small-sized elongated grains, characteristic of the cold-working conditions, were observed near the interface while medium-sized regular ones were identified in areas immediately after the Al/Fe interface until to the specimen boundaries. As concern the AA1050 side, the micro-structure consisted of insoluble $FeAl_3$ particles (dark constituent) dispersed in the aluminium matrix (lighter constituent), as Figure 3-F shows. The morphology of these particles seemed to be not influenced by explosion welding.

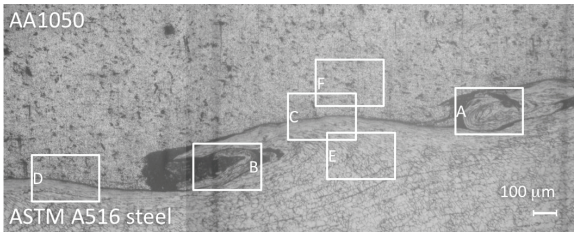

Fig. 3. Details of Al/Fe interface (as-clad condition).

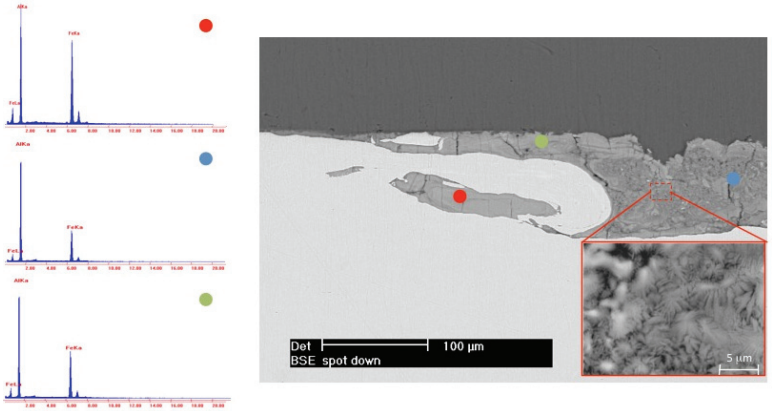

Fig. 4. SEM Observation.

The heat-treated specimens were accurately examined to measure changes in Al/Fe interface. A well-designed measurement process, divided into calibration, acquisition and computation steps, was applied to quantify the extension of the inter-metallic phases along the Al/Fe interface. The micro-structural measurements involved the use an optical microscope connected to a digital camera and a computerised image tool. At the end of the acquisition process, the entire Al/Fe interface of the specimen was captured by shooting multiple images at different locations, performing the brightness/contrast adjustment, joining them in a single frame and finally over-laying a 100 µm grid (Figure 5).

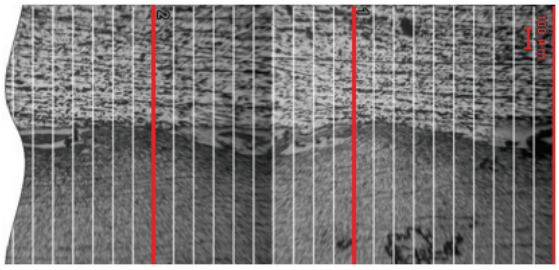

Fig. 5. Al/Fe interface with grid.

In the measurement step, the presence of inter-metallic phases was evaluated for each sector of 100 μm length. These phases, darker than aluminium and lighter than ferrite, were searched at interface. In case of a not very clear distinction between light and dark zones, the inter-metallic phases were considered as not present. The above procedure was repeated for all specimens and the results reported in Table 3 in terms of real inter-metallic extension and percentage respect to the entire specimen length of 13 mm.

Specimen ID	Temperature (°C)	Time (minutes)	Fe_xAl_y length	
			(mm)	(%)
1	100	5	5.4	41.54
2	100	25	6.1	46.92
3	500	5	12.4	95.38
4	500	25	12.9	99.23
5	300	15	5.7	43.85
6	300	15	6.7	51.54
7	300	15	5.4	41.54
8	300	15	7.1	54.62
9	300	15	6.0	46.15
10	300	0.86	5.2	40.00
11	300	29.14	6.6	50.77
12	17.16	15	5.9	45.38
13	582.4	15	11.5	88.46

Table 3. Inter-metallic extensions.

The expected outcome was the increase of the inter-metallic layer length with the increase of both temperature and time. The analysis of variance (ANOVA) of the Fe_xAl_y length response variable pointed-out the temperature as the main factor influencing the extension growth of the inter-metallic phases along the Al/Fe interface while time was negligible (Table 4).

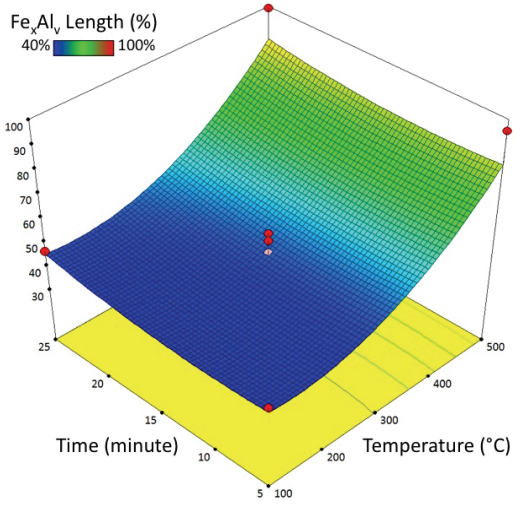

Fig. 6. Fe_xAl_y extension.

Source	SS	DF	MS	F	Prob>F
Model	80.62	5	80.62	8.69	0.0065
Temperature	58.97	1	58.97	31.79	0.0008
Time	0.95	1	0.95	0.51	0.4976
Temperature·Time	10^{-2}	1	10^{-2}	$5.4 \cdot 10^{-3}$	0.9435
Temperature^2	20.49	1	20.49	11.05	0.0127
Time^2	1.07	1	1.07	0.57	0.4732
Residual	12.99	7	1.86		
Total	***93.60***	***12***			

Equation of the Response Surface

Fe_xAl_y Length=+6.221-1.179·10^{-2}·Temperature -7.550·10^{-2} ·Time-2.5000·10^{-5} ·Temperature·Time+4.291·10^{-5}

Table 4. ANOVA – Inter-metallic extensions.

The good agreement between experimental and predicted results was confirmed by the high value of R^2 and adjusted R^2 of the quadratic model, respectively more than 86% and 76% (Figure 6). The experimental data highlighted that the specimens exposed to a thermal stress for temperatures below 300 °C did not exhibited a significant growth of the inter-metallic band extension respect to the as-clad specimen. The extension of inter-metallic phases covered less than 50% of the entire specimen Al/Fe interface length and the interface consisted of unconnected ripples and sacks. The situation drastically changed in case of specimens submitted to temperature equal or greater than 500 °C. The Al/Fe extension was more than 88% of the entire, sometimes covering the entire interface. The aspect of the interface was constitute by ripples and sacks connected by a continuous thin band of inter-metallic phases (Figure 7).

Fig. 7. Al/Fe interface (specimen ID 13).

Based on above observations, the analysis was extended to measure the inter-metallic layer thickness of the specimens subjected to the temperature of 500°C (ID 3 and 4). The measurement process previous applied for Fe_xAl_y extension was adapted by mounting 25x objective and 20x eyepieces lenses into the microscope, acquiring multiple images of the Al/Fe interface. Five shots per specimen were randomly selected and two grids of 10 μm spacing were over-laid for computing inter-metallic thickness of each shot, for a total number of measurements per specimen equal to 50. The results achieved pointed out the importance of the time variable on inter-metallic thickening. In fact, the average Fe_xAl_y layer thickness of specimen ID 3 (Temperature=500°C and time=5 min) was equal to 5.58 μm, quite an half of the average thickness of specimen ID 4, equal to 11.23 μm, subjected to the same temperature for a total time of 25 minutes. The observations of Fe_xAl_y growth and thickening were very important to justify the application of laser welding. In fact during

laser welding, the high thermal input is localised in very narrow zone and the high travel speeds of the laser beam minimise the heat conductivity into the surrounding metal. The Fe_xAl_y layer should become larger and thicker in area just below laser beam while it should remain quite the same dimensions in areas away from laser beam.

5. Micro-hardness evaluation of heat treated specimens

Micro-hardness test were performed to measure the strength of Al/Fe interface in a non-destructive way as well as its variation under heat thermal loads. A Vickers micro-tester (HX-1000TM of REMET) mounting a 40x objective and 15x eyepieces lenses was used, setting the indentation load to 200 g for 15 s, in compliance with ASTM standard E92. Analysis points were sufficiently spaced to eliminate the effect of neighbouring indentations while evaluating existing materials and phases. Five indentations were taken at specific locations at and far from Al/Fe interface (Figure 8) for three times and results then averaged.

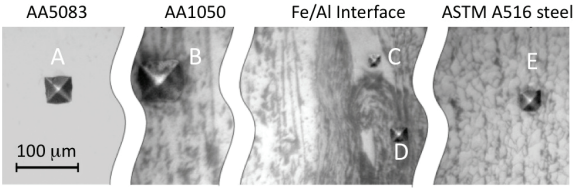

A=+ 3.2 mm
B =+ 1.0 mm
C =+ 0.0 mm
D =- 0.1 mm
E = - 1.5 mm

Fig. 8. Vickers indentations.

The area of measure was randomly selected for each specimen by respecting the condition that at least one ripple was contained in it. The hardness result was the average value of all inter-metallic phases embraced by the indenter diagonal. The results of Table 5 pointed-out that hardness values of AA5083, AA1050 and ASTM A516 steel were slightly affected from heat treatments. The justification of this behaviour could be that longer time at investigated temperatures should be necessary to allow greater diffusion fluxes. The hardness of the inter-metallic compounds (point C) was greatly influenced by temperature and time factors.

Specimen ID	Temperature (°C)	Time (minutes)	Indentation ID (HV)				
			A	B	C	D	E
1	100	5	105	46	583	266	195
2	100	25	107	41	534	245	178
3	500	5	81	31	430	242	182
4	500	25	83	28	483	239	166
5	300	15	91	44	554	235	186
6	300	15	81	45	593	238	180
7	300	15	97	44	618	247	183
8	300	15	89	42	582	278	175
9	300	15	81	39	582	294	183
10	300	0.86	107	43	543	246	186
11	300	29.14	85	40	527	245	174
12	17.16	15	100	41	545	246	179
13	582.4	15	72	30	476	192	158

Table 5. Vickers results.

The analysis of variance (ANOVA) of the inter-metallic hardness response variable pointed-out that increases in time and temperature lower hardness (Figure 9). In particular, temperature square, followed in order of importance from temperature and time square, were the main significant terms of the quadratic model (Table 6). This model presented R^2 and adjusted R^2 values equal to 88% and 79%. The reduction in hardness could be caused by the inter-metallic transformation from hard to soft phases. The fragility of the inter-metallic layers was also witness from the cracks present inside inter-metallic ripples. The investigated specimen, exposed to 300°C for 15 minutes in compliance with as-simulated condition, was characterised by the presence of cracks localised caused only by mechanical polishing.

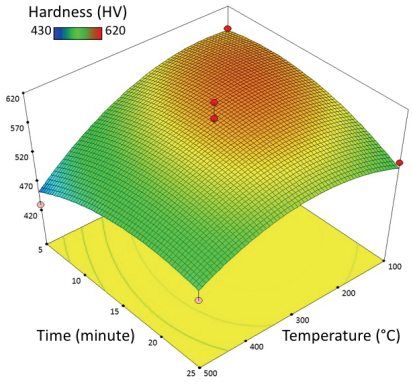

Fig. 9. Inter-metallic hardness.

Source	SS	DF	MS	F	Prob>F
Model	27854.0	5	5570.81	11.75	0.0027
Temperature	8916.54	1	8916.54	18.81	0.0034
Time	34.79	1	34.79	0.07	0.7942
Temperature·Time	4726.56	1	4762.56	9.97	0.0160
Temperature^2	10780.7	1	10780.7	22.75	0.0020
Time^2	5084.84	1	5084.84	10.73	0.0136
Residual	3317.41	7	473.92		
Total	***31171.4***	***12***			

Equation of the Response Surface

HV of Point C=+560.674+1.658·10^{-1} ·Temperature +3.165 ·Time-1.719·10^{-2} ·Temperature·Time-9.842 ·10^{-4} ·Temperature^2-0.270·10^{-1} ·Time^2

Table 6. ANOVA – Vickers Results of Point C.

6. Mechanical strength of heat treated specimens

STJ specimens for mechanical evaluation were fabricated with machining processes from Al/Fe STJ (Figure 10) in compliance with ASTM A264–03 standard by removing the majority of the weakest clad materials (AA5083 and AA1050) and leaving a small nub with

length w and thickness α. The ratio between w and α was 1½ with the maximum allowed dimension of w equal to 3.18 mm (⅛"). Other important dimensional features were the specimen width equal to 25.40 mm (1"), length equal to 63.50 mm (2½"), distance between side surfaces equal to 19.05 mm (¾") and minimum steel thickness t greater than 2w. The heat treatments of these specimens were performed by following the same temperature-time parameters of those defined for the CCD experimental plan of the metallographic evaluation.

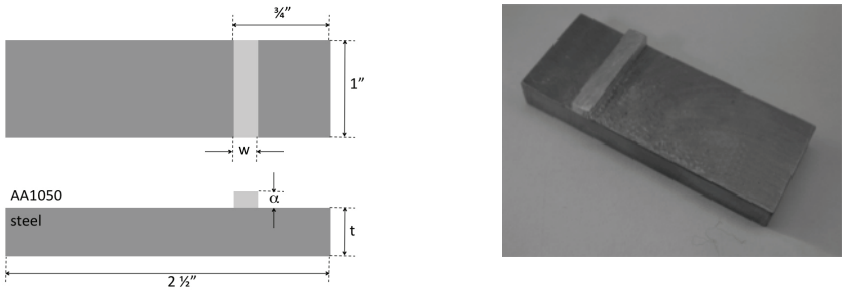

Fig. 10. Shear test - Specimen.

Shear test was very important to assess transition joint technical conformity by measuring the maximum shear strength of the bond interface and comparing it to the maximum shear strength of the weakest material of the STJ. The shear strength of the test piece was defined as the peak shearing load divided by the sheared area. Interfacial bonding of the clad specimen was evaluated by shear stress measured with a universal test machine INSTRON 4485 with a 200 KN loading cell and a home designed testing equipment in which the test piece and the jig were fitted, assuring the easy specimen blocking and high positioning accuracy as well as flexibility of use for other required tests. The shear test were performed with the mobile crosshead moving at 3.0 mm/min. The evolution of stress-displacement curve initially presented a rapid increase of the stress value, its stabilisation and finally its rapid reduction. The rupture was localised in the AA1050 and not at interface AA1050/steel, justifying the trend of this loading curve (specimen BM in Figure 11). The same figures reports the loading curves of specimen ID 8, heated at 300°C for 15 minutes, and specimen ID 4, heated at 500°C for 25 minutes.

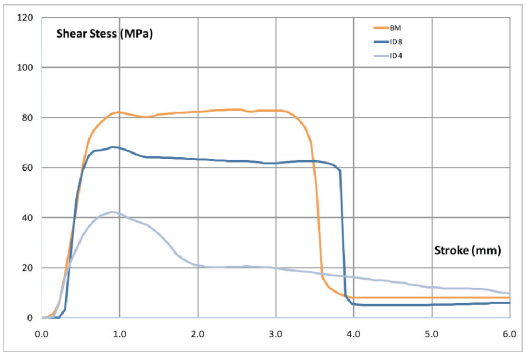

Fig. 11. Loading curve of heat treated specimens.

As figure shows, the shear strength decreased with the increase of both processing temperature and time, causing the rapid lowering of the maximum shear stress values. This trend was also confirmed by analysing the other tests.
Table 7 reports the final results of all tests in term of maximum values of the shear stress. All stress values recorded during tests were decidedly higher than 50-60 MPa prescribed from Lloyd's Register of Shipping, revealing the good fabrication quality of the observed STJ. The worst results were achieved when specimens were subjected to high temperature for a long time (Specimens ID 4 & 13).

Specimen ID	Temperature (°C)	Time (minutes)	Shear stress	
			(MPa)	Lloyd's
1	100	5	69.57	Positive
2	100	25	70.37	Positive
3	500	5	75.95	Positive
4	500	25	44.50	Negative
5	300	15	80.64	Positive
6	300	15	72.09	Positive
7	300	15	70.52	Positive
8	300	15	69.73	Positive
9	300	15	71.63	Positive
10	300	0.86	73.65	Positive
11	300	29.14	69.79	Positive
12	17.16	15	69.57	Positive
13	582.4	15	5.56	Negative

Table 7. Shear stress values.

The analysis of variance (ANOVA) of the shear stress response variable pointed-out that increases in time and temperature lowering shear strength (Figure 12). In particular, temperature, followed in order of importance from temperature square and time, were the main significant terms of the quadratic model (Table 8). This model presented R^2 and adjusted R^2 values equal to 78% and 63%.

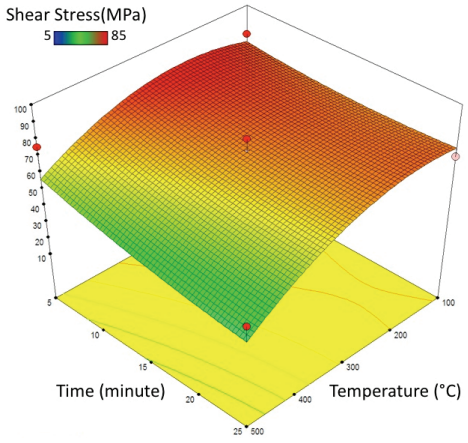

Fig. 12. Shear stress.

Source	SS	DF	MS	F	Prob>F
Model	3626.63	5	725.33	5.04	0.0281
Temperature	1512.87	1	1512.87	10.52	0.0142
Time	163.00	1	163.00	1.13	0.3224
Temperature·Time	260.02	1	260.02	1.81	0.2207
Temperature^2	1578.79	1	1578.79	10.98	0.0129
Time^2	28.21	1	28.21	0.20	0.6712
Residual	1006.53	7	143.79		
Total	***4633.16***	***12***			

Equation of the Response Surface

Shear Stress=+52.815+2.177·10^{-1} ·Temperature+1.537·10^{-1} ·Time-4.031·10^{-3} ·Temperature·Time

Table 8. ANOVA – Shear stress values.

Some interesting considerations were performed by comparing results of shear stress (Figure 12), inter-metallic extension (Figure 6) and micro-hardness (Figure 9). The behaviour of the shear stress response surface was opposite to that of the inter-metallic extensions. In particular the highest and lowest values of the shear stress was achieved for the lowest and highest temperatures, respectively. On the contrary the highest and lowest values of the inter-metallic extension were achieved for the highest and lowest temperatures. For this reason it was possible to suppose that shear strength decreased with the increase of the inter-metallic length. In contrast, the relation between shear stress and inter-metallic hardness was not so clearly evident. In fact the highest and lowest values of the shear stress were achieved for the lowest and highest temperature-time couple. However in the other areas this trend was not quite evident and further investigation will be necessary. Based on the above results, it was possible to suppose that the main cause of the lowering of the shear strength with the temperature increase was the inter-metallic layer growth, even if the inter-metallic phases become softer.

The strength of the welding zone is evaluated by Ram Tensile Test. During the test, the force is applied to the direction perpendicular to the planes delimiting different material interface. A specimen with a particular parallelepiped/cylindrical shape is used in order to concentrate stresses in the section just above the transition area that corresponds to the bond interface, as Figure 13 shows. The MIL-J-24445A standard, specifies maximum dimensions of the bi-material specimen but its principles can be easily extended to tri-material joints. In this last case, the strength of the steel/AA1050 bond interface is estimated rather than that of the AA5083/AA1050 one. The specimen, punch and matrix prescribed by the above cited standard are reported in Figure 14, together with the designed testing equipment. The matrix is fixed while the punch moves in contact with the bond interface, compressing it until rupture. The MIL-J-24445A standard does not give values or suggestions linked to testing parameters (e.g. punch speed) and/or specimen clamping. The specimen is simply rested on the matrix top surface, allowing its rotation around the cylindrical axis. In the hypothesis that the pressure between punch and specimen during contact is uniform, the applied load can be considered as axial-symmetric. The thickness D of the bond zone is always equal to 1.72±0.1 mm, independently from the values of steel and aluminium thicknesses. The thickness D is achieved by simply varying the hole depth. The testing

equipment, designed and realised in compliance with the MIL-J-24445A standard, allowed the easy set-up on an universal tensile testing machine. The designed equipment consisted of a screwed punch and a two elements matrix with a changeable cylindrical insert. The punch is mounted on the top mobile crosshead of the INSTRON 4485 machine while the matrix is fixed to the machine basement with bolts and nuts. The choice of the changeable insert was justified by the need to substitute the insert in case of high wear conditions as well as to select the proper tolerance gap with the specimen. The correct alignment between the punch and specimen axes to avoid bending effects was realised by means of a guided groove in the low part of the matrix. The pressure of the punch caused tensile loads on specimen bond interface. The maximum tensile stress value recorded during test was used to assess the joint strength for several temperature-time cycles. The minimum value of the tensile stress to consider the joint as good should be greater than 75 N/mm^2.

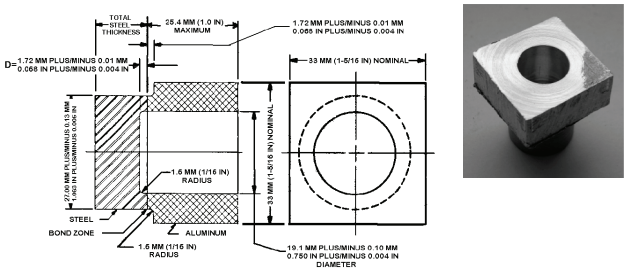

Fig. 13. Ram test specimen.

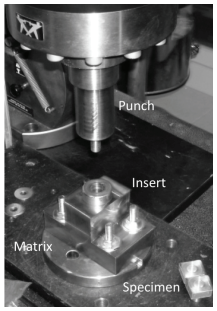

Fig. 14. Testing equipment

The designed experimental plan for mechanical testing was extended respect to the plan used for micro-hardness evaluation to preserve continuity with previous investigation, evaluate more critical conditions associated to higher time and/or temperatures and improve knowledge about mechanical strength limits of tri-material transitions joints. Metallographic examinations revealed that the heat-treated joints properties remained quite equal to those of as-clad specimen for temperatures lower than 300 °C and processing times lower than 15 minutes. The new experimental plan is reported in Table 9, in terms of temperature-time couples. The punch speed was set to 0.05 mm/s for all tests.
Some important considerations can be carried-out by analysing these results. The maximum strength of the as-clad specimen as well as specimens processed at 300 °C were greater than

minimum value of 120 MPa certified by the material supplier. In addition, the specimen resistance was mainly supported by the small thickness of AA1050, considering that the maximum strength of this commercial alloy was about 180-190 MPa at high cold work conditions. These values suggested that the thermal cycles may reduced the cold work conditions, with consequent reduction of the maximum strength of the tri-material joint. The specimen behaviour changed when processing temperature was greater than 300°C. Based on the above results, temperature was the main factor causing the lowering of the specimen mechanical strength.

Specimen ID	Temperature (°C)	Time (minutes)	Tensile	
			Force (KN)	Stress (MPa)
HTRT1	25	5	29.4	233.7
HTRT2	300	15	30.1	239.3
HTRT3	500	25	4.3	34.2
HTRT4	300	25	25.2	200.3
HTRT5	400	20	16.4	130.4
HTRT6	500	15	4.8	38.2
HTRT7	500	5	17.8	141.5
HTRT8	25	25	29.9	237.7

Table 9. Ram tensile test values.

The same considerations arose from the analysis of the load-displacement data. HTRT1 and HTRT2 specimens were characterised by the same curves, with equivalent values of the maximum load and displacement, as Figure 15 reports. This behaviour pointed-out that mechanical properties were not greatly altered from processing temperature and time, even if HTRT2 specimen stayed in the oven at 300°C and HTRT1 specimen was thermally untreated. The maximum supported load started to drop when specimen were treated at temperatures higher than 300 °C. The HTRT5 specimen, processed at 400 °C for 20 minutes, and HTRT7 specimen, processed at 500 °C for 5 minutes, were accomplished by the reduction of the maximum load value with the increase of the maximum displacement (Figure 16). In fact, the load-displacement curves of the two specimens were perfectly equivalent from the mechanical point of view. The maximum load drastically drop for higher temperatures, as HTRT3 specimen, processed at 500 °C for 25 minutes, witnessed.

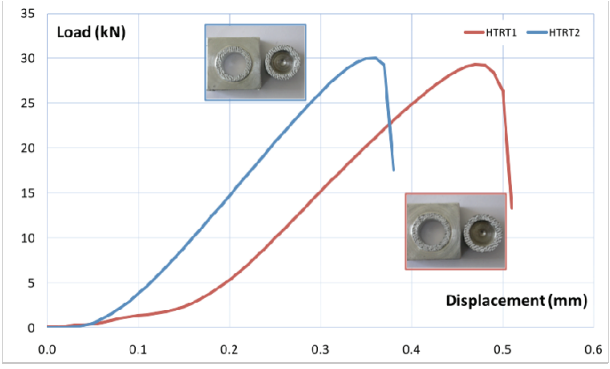

Fig. 15. Load/displacement curves of HTRT1 and HTRT2 specimens.

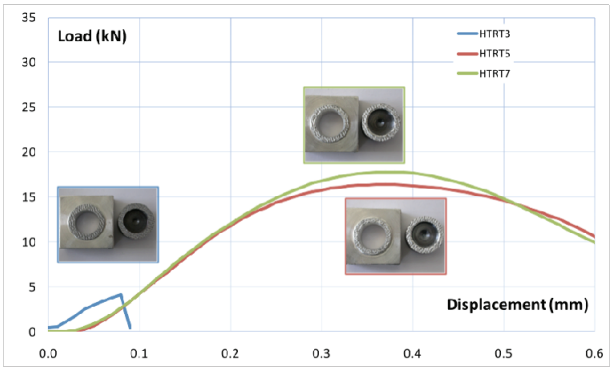

Fig. 16. Load/displacement curves of HTRT3, HTRT5 and HTRT7 specimens.

The reduction of the mechanical strength with temperature and time becomes more evident with results reported in Figure 17, the ANOVA of which is reported in Table 10.

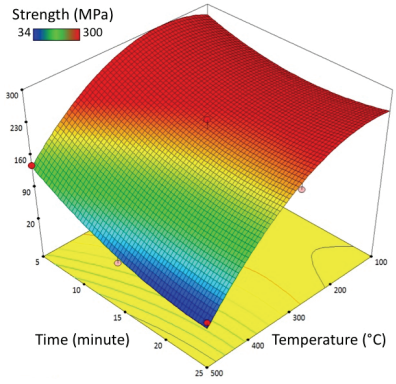

Fig. 17. Ram tensile test.

Source	SS	DF	MS	F	Prob>F
Model	50191.0	5	10038.2	20.21	0.0478
Temperature	26285.5	1	26285.5	52.91	0.0184
Time	3962.75	1	3962.75	7.98	0.1058
Temperature·Time	3391.77	1	3391.77	6.83	0.1205
Temperature^2	12417.8	1	12417.8	25.00	0.0378
Time^2	951.94	1	951.94	1.92	0.3005
Residual	993.55	7	496.77		
Total	***51184.5***	***12***			

Equation of the Response Surface

Shear Stress=253.66+8.388·10^{-1}·Temperature-8.341 ·Time-1.218·10^{-2} ·Temperature·Time-1.876·10^{-3} ·Temperature^2+2.842·10^{-1} ·Time^2

Table 10. ANOVA – Ram tensile test values.

The justification of this fragile behaviour was that the heat treatment at high temperature promoted the inter-metallic redistribution at Al/Fe bond interface, with consequence growth of the inter-metallic thickness, causing the lowering of the mechanical properties. This hypothesis has been confirmed by previous works (*Tricarico et al., 2007*) in which the influence of the thermal loading of the Al/Fe explosion welded joints was investigated by measuring the extension and thickness of inter-metallic compounds at Al/Fe interface. The metallographic analysis measurements have pointed-out that the band extension was mainly influenced by the temperature because the increase of the band extension with increasing temperature has been recorded. Observing the evolution of the inter-metallic band thickness, it has been observed that thickness at 500°C after 5 minutes was half than that obtained after 25 minutes.
Another important aspect took into account was the shape of the fractured surfaces of the thermally loaded specimens. The fracture surfaces were characterised by a ductile fracture with very low appreciable deformation and/or absent signs of gross plastic deformation. This fracture may be justified by the presence of a continuous diffuse inter-metallic layer that triggered micro-cracks. The Figure 18 reports the fractures aspects of HTRT1, HTRT2 and HTRT3 specimens. The pattern of the HTRT1 specimen is very irregular with evident differences between peaks and voids. These difference between peaks and voids were lower in case of HTRT3 specimen, as the fragile fracture of the specimen at the end of the test shows. The surface aspect of the HTRT2 specimen seemed to be intermediate between the other two specimen surfaces, corroborating results achieved during the ram tensile test in terms of maximum load and displacement.

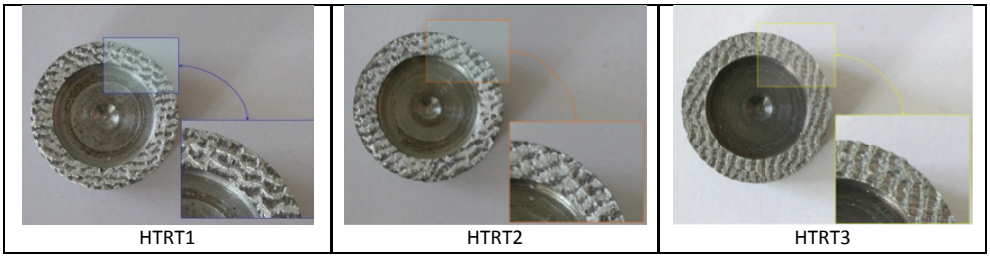

Fig. 18. Surface fractures of HTRT1, HTRT2 and HTRT3 specimens.

7. Bead on plate

Welding tests on STJs were performed on specimens machined from the same bar, which section and length were 26.3·26.0 mm² and 1000.0 mm respectively. The materials of the STJ bar were steel - ASTM A516 grade 55 - and aluminium alloys - AA1050 and AA5083, the thicknesses of which were 13.7±0.4 mm for steel and 11.7±0.3 mm for aluminium alloys. Bead-on-plate were carried-out by using process parameters identified in the previous preliminary analysis and varying only the joint geometry. In this way, the laser-induced thermal load was kept constant on the top surface while Al/Fe interface was subject to different thermal stresses due to the reduction of the specimen thickness. To achieve this result, upper section interacting with the laser beam was machined to reduce the distance d between the fused zone and bond interface. For this reason specimens with different thicknesses were employed. The specimen length, equal to 80.0 mm, was chosen to achieve

stationary conditions during welding. Some trial tests on STJ specimens were performed to verify if the main geometrical parameters of weld sections were the same of those achieved in the preliminary analysis on the base materials. Weld geometry was characterised by the penetration depth and width equal to 5.4 and 5.0 mm, quite equal to those measured on the base materials. The small variations between results were inputted to the laser beam power fluctuation, specimen geometry (plate vs. bar) as well as materials compositions (mono-material vs. tri-materials).

The following tests on STJs were performed with the laser beam power equal to 4.3 kW and travel speed set to 1.5 or 1.0 m/min respectively for aluminium or steel top surface. The specimen LPBAL1, LPBAL2 and LPBAL3 were realised by machining the aluminium side (Table 11). The distance d between the melt zone and the Al/Fe was planned to 3.0, 1.5 and 0.0 mm, assuming that the penetration depth remained constant to 5.5 mm. Table 11 also reports cut section, details of the weld fused area and geometrical parameters such as the penetration depth h and width r. In particular, these two parameters decreased with the reduction of the distance d, in spite of the thermal load on the top surface was the same for all specimens.

Specimen	LPBAL1	LBPBAL2	LBPBAL3
Geometry	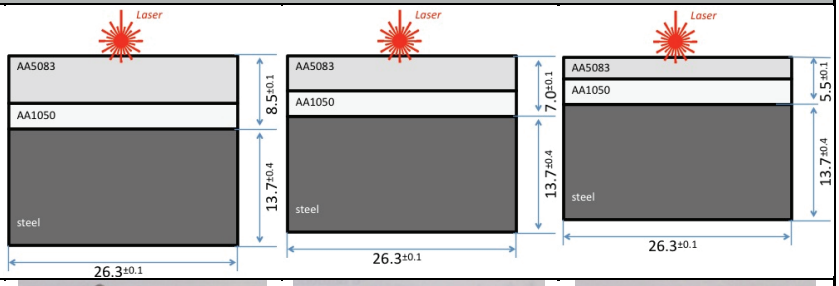		
Results	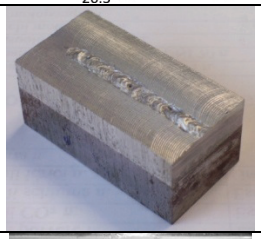	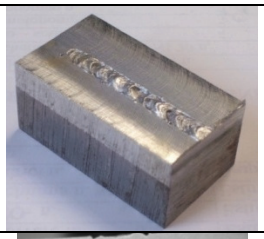	
Section	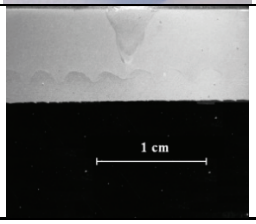	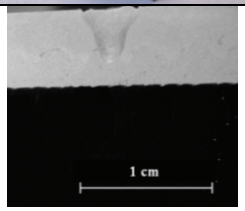	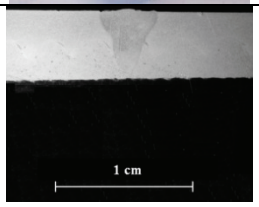
Parameters	r = 4.8 mm \ h = 5.1 mm	r = 4.7 mm \ h = 4.6 mm	r = 4.7 mm \ h = 4.5 mm

Table 11. Tests on STJs – Aluminium side.

Possible justifications of this trend were the lower conductivity of steel, that reduced the heat transmission at bond interface as well as in the steel region, and the smaller aluminium thickness, that lowered the possibility of the laser-induced heat to quickly went away from the weld fused area. The decrease of the main weld parameters become more evident by comparing the as-clad specimen with LPBAL3. The difference of the penetration depth between these two specimen was equal to 0.9 mm while the difference of the penetration width was equal to 0.3 mm.
The same experimental framework was applied for specimen welded from the steel side. The specimen LPBST1, LPBST2 and LPBST3, realised by the steel side, were machined from the same bar of the specimen processed from the aluminium side to eliminate differences due to manufacturing batch. The distance d between the melt zone and the Al/Fe was planned to 3.0, 1.5 and 0.0 mm, assuming that the penetration depth remained constant to 5.0 mm. Table 12 reports specimen dimensions, cut section, details of the weld fused area and geometrical parameters such as the penetration depth h and width r. The reduction of penetration depth h and width r with the decrease of the distance d were also detected for these tests but this reduction was considered as negligible.

Specimen	LPBST1	LPBST2	LPBST3
Geometry	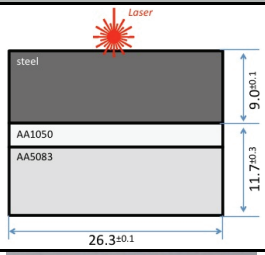	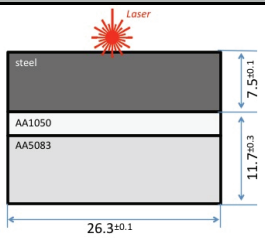	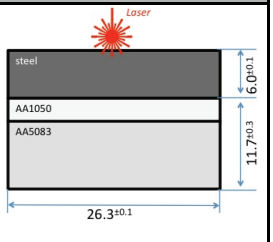
Results	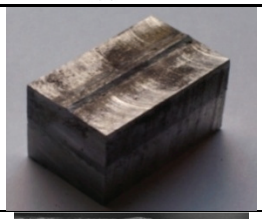		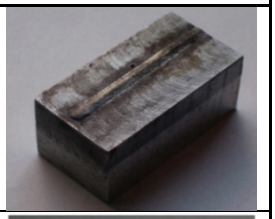
Section	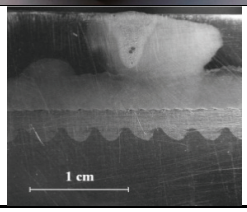	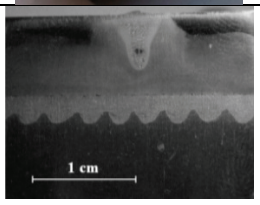	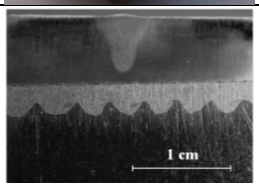
Parameters	r = 4.8 mm \ h = 5.4 mm	r = 5.1 mm \ h = 5.3 mm	r = 5.0 mm \ h = 5.2 mm

Table 12. Tests on STJs – Steel side.

8. Metallographic examination of bead on plate specimens

The study of microstructure of the bond interface was manly addressed to the qualitative and quantitative analysis of the Al/Fe inter-metallic film in terms of variation of its

extension and thickness. The procedure was the same of that used for the heat treated specimens. The results of the metallographic examinations are reported in Table 13 in terms of the reference length L_{REF} and the inter-metallic extension L_{INT} as well as the ratio between these two measurements. The reference length LREF, equal to 15.0 mm, was the same for all specimens. The results pointed out that the inter-metallic extension L_{INT} was greater than 50% of the total length L_{REF} of the cut section in the as-clad specimen. The length L_{INT} increased with the decrease of the distance d between weld fused area and bond interface. This increase was more rapid for specimens welded from the steel side than those welded from the aluminium side. Another important aspect to underline was that the two main factors linked to ripples and film growth contributed to the inter-metallic extension value. Ripples existed in the as-clad specimen, as the main feature of the explosion welding process. The laser-induced heat loads influenced inter-metallic ripples, promoting their growth by inter-diffusion, but no new ripples were created during welding. The inter-metallic film was mainly promoted by laser-induced thermal loads because it also aroused in areas in which it did not exist at all. The contribution of the inter-metallic film was by made more evident by the L_{FILM}/L_{REF} ratio in Table 13. The enlargement of the inter-metallic film was also in this case higher for specimens welded from the steel side.

Specimen ID	Condition	Distance	Length		Ratio	
		d (mm)	L_{REF} (mm)	L_{INT} (mm)	L_{INT}/L_{REF}	L_{FILM}/L_{REF}
--	As-clad	--	15.0	8.4	56.0	8.0
LPBAL1	Welded from aluminium side	3.0	15.0	8.4	56.0	8.4
LPBAL2		1.5	15.0	8.4	56.0	8.6
LPBAL3		0.0	15.0	8.9	59.3	10.9
LPBST1	Welded from steel side	3.0	15.0	8.4	56.0	8.4
LPBST2		1.5	15.0	9.5	63.3	14.7
LPBST3		0.0	15.0	10.4	69.3	16.1

Table 13. Inter-metallic extension.

The inter-metallic film thickness was evaluated in terms of average value of several random measures near the fused area. The maximum and the minimum thicknesses were also evaluated (Table 14), considering that these values were representative of local conditions. The evaluation of the average value of the film growth made observations independent of the previous state of the as-clad material, linking results to the effects of the laser induced heat.

Specimen ID	Condition	Distance	H_{FILM}			Film
		d (mm)	Max (μm)	Avg (μm)	Min (μm)	Growth
--	As-clad	--	10.29	6.51	3.10	--
LPBAL1	Welded from aluminium side	3.0	17.45	8.11	3.51	25%
LPBAL2		1.5	14.07	8.27	4.58	27%
LPBAL3		0.0	17.70	8.95	3.01	38%
LPBST1	Welded from steel side	3.0	11.53	7.30	3.92	12%
LPBST2		1.5	10.65	7.40	3.43	14%
LPBST3		0.0	11.05	8.21	5.53	26%

Table 14. Inter-metallic film thickness.

The average film thickness increased with the reduction of the distance d with the same trend independently form the material of the welding side. The increase of film thickness was greater for specimen welded from the aluminium side than those welded from the steel side. This behaviour, opposite to that recorded for the film extension growth, pointing out that laser induced heat remained on aluminium side of the tri-material specimen because steel created a thermal barrier with its lower thermal conductivity.
The SEM analyses were then performed from the qualitative point of view by visually inspecting morphology of the Al/Fe interface. The back-scattered electron (BSE) images near the specimen Al/Fe interface showed the AA1050 in dark grey, the ASTM A516 steel in the light grey the "wavy" interfacial area with different grey, in function existing Fe_xAl_y inter-metallics. Figure 19 is one of the acquired BSE images for the specimen LPBAL1, welded from the aluminium side. The analysis in three different positions inter-metallic compounds were more numerous and fragile, as figures show. Figure 19 also reports the results of the micro-analysis of the area indicated from the three shapes (circle, rectangle and triangle). With energy dispersive x-ray spectrometers (EDS), chemical compositions was determined quickly. Despite the ease in acquiring x-ray spectra and chemical compositions, the potentially major sources of error were minimised by optimising the operative conditions necessary to improve the statistical meaning of the electron counter. In particular, the scanning area was equal to 1 μm², the incident energy was 25 keV on the specimen surface with a working distance of 10 mm (in this way the x-ray take-off distance was equal to 35°), the electronic current was tuned in order to generate a X-ray counter rate of 2000 pulse per second and the effective counter time was equal to 100 s (*Capodiceci*, 2007). Figures 20-23 reports the SEM analyses for specimen LPBAL3, LPBST1 and LPBST3. It is evident that the number of grey level was higher for specimen welded form the steel side than the aluminium one. This experimental evidence was probably due by the lower conduction coefficient of steel than that of aluminium, which caused heat to be slowly removed after welding

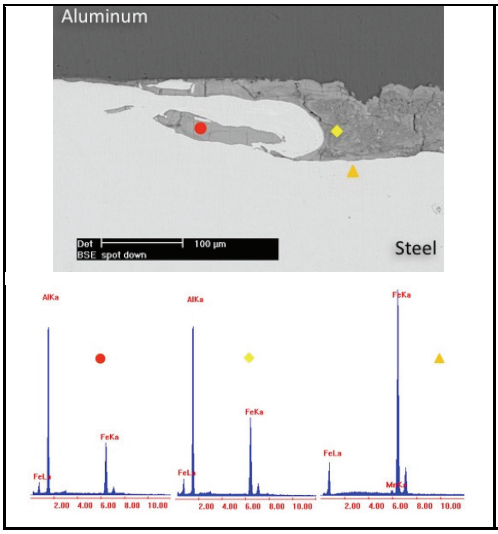

Fig. 19. SEM analysis – LPBAL1.

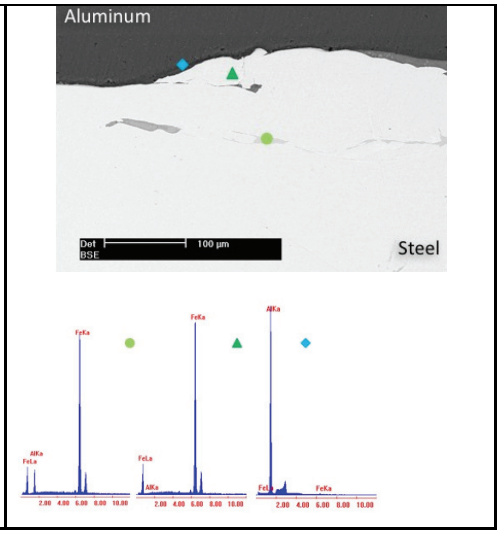

Fig. 20. SEM analysis – LPBAL3.

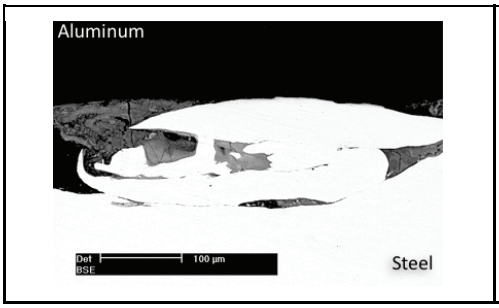

Fig. 21. SEM analysis – LPBST1.

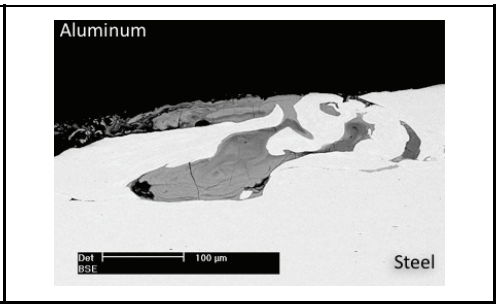

Fig. 22. SEM analysis – LPBST3.

9. Mechanical strength of laser welded specimens

The mechanical characterisation of the welded specimens allowed the modifications to the mechanical properties (shear and tensile strengths) caused by laser beam interaction to be evaluated. Shear and ram tensile samples were achieved from the same plate with the sampling scheme shows in Figure 23 in order to avoid difference in STJ lot characteristics. The laser beam passed at the centre of the small nub of the shear test specimens and sufficient far from the ram tensile specimens. The area of the small nub of the shear specimens were consequently subjected to the highest thermal stresses while the bonding area AA1050/steel of the ram tensile specimens were uniformly thermally loaded. The process parameters used for bead-on-plate welds were the same of those employed for STJ bars in the previous experimental step. Increasing thermal loads at the bond interface were achieved by removing material from the surface interacting with the laser beam. The reduction of the plate thickness required the scaling down of specimen dimensions for some samples. Table 8 and Table 9 report the dimensions of shear and ram tensile test specimens. An additional test specimen was cut at the centre of the plate to evaluate the maximum welding penetration depths in comparison with those of the welded bars as well as hardness values (*Tricarico et al, 2007*).

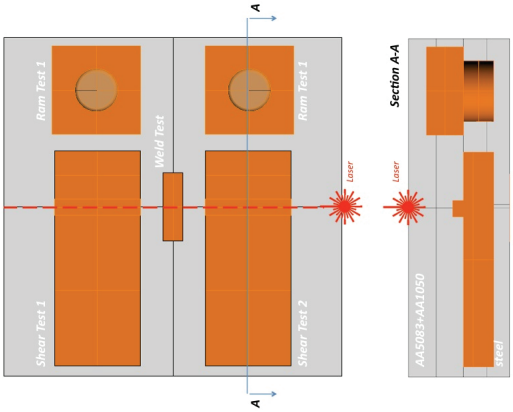

Fig. 23. Specimen sampling.

The shear test were performed with the mobile crosshead moving at 3.0 mm/min. The acquisition of several high resolution digital images during tests was useful to visually understand the mechanisms of deformation of the small nub (Figure 24), compared with numerical data.

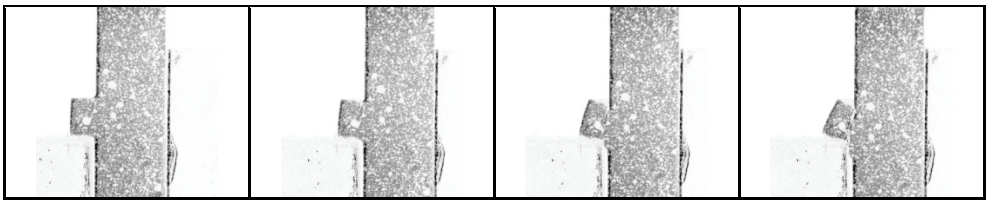

Fig. 24. Deformation times of sample B1.

The two repetitions for each welding conditions were characterised by load-displacement curves wholly overlaid, as Figure 25 shows for sample B1 and B2. The evolution of stress-displacement curve initially presented a rapid increase of the stress value, its stabilisation and finally its rapid reduction. The rupture was localised in the AA1050 and not at interface AA1050/steel, justifying the trend of this loading curve.

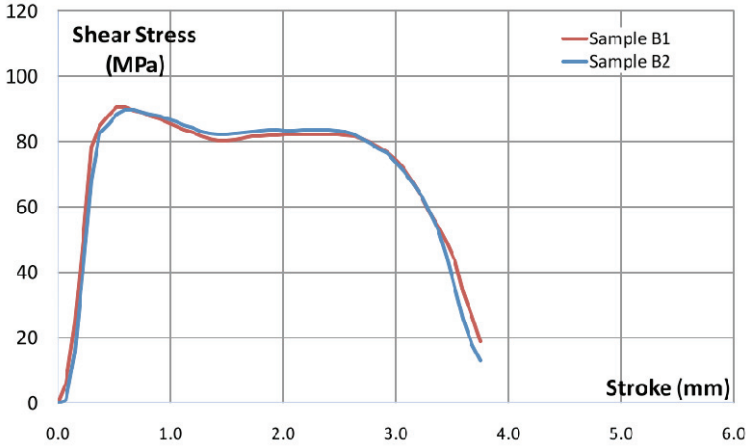

Fig. 25. Shear stress vs. punch stroke of sample B1 and B2.

Table 15 reports the final results of all tests in term of maximum shear load and stress. All stress values recorded during tests were decidedly higher than 50-60 MPa prescribed from Lloyd's Register of Shipping, revealing the good fabrication quality of the observed STJ. Results also pointed-out that the reduction of the specimen thickness and the consequent reduction of the distance between weld fused area and bond interface caused the decrease of the maximum shear strength.

Specimen ID	Condition	Al/Fe thick	Geometry			Shear	
		mm/mm	α (mm)	w (mm)	t (mm)	T (KN)	τ (MPa)
-- / A1-A2	As-clad	11.7/13.7	3.00	4.50	9.00	10.0	87.4
LPBAL1 / B1-B2	Welded from aluminium side	8.5/13.7	3.00	4.50	9.00	10.1	88.3
LPBAL2 / C1-C2		7.0/13.7	3.00	4.50	9.00	9.3	81.7
LPBAL3 / D1-D2		5.5/13.7	3.00	4.50	9.00	9.0	78.7
LPBST1 / E1-E2	Welded from steel side	11.7/9.0	3.00	4.50	9.00	10.0	87.4
LPBST2 / F1-F2		11.7/7.5	2.50	3.75	7.50	8.8	86.6
LPBST3 / G1-G2		11.7/6.0	2.00	3.00	6.00	6.3	83.0

Table 15. Shear test – Sample dimensions & results.

This decrease was more evident for specimen welded from the aluminium side than those welded from the steel side, as Figure 26 and Figure 27 show.

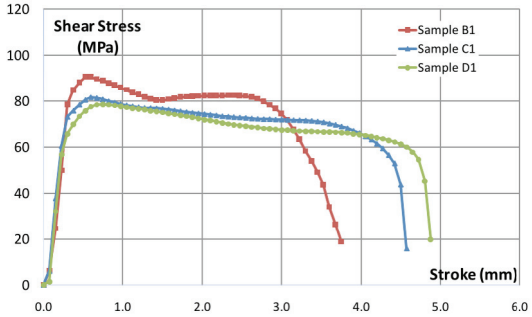

Fig. 26. Samples B1, C1 and D1.

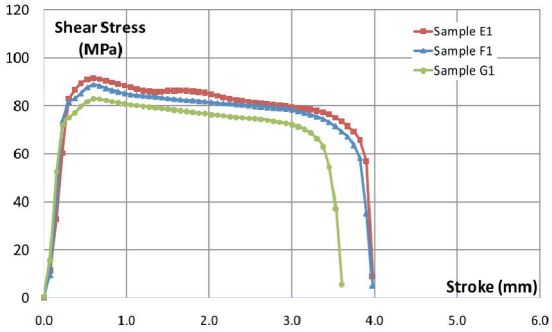

Fig. 27. Samples E1, F1 and G1.

The ram tensile test were then carried-out. Two repetitions for each welding condition was useful to assess test repeatability. Figure 28 reports results of the samples RA1 and RA2, in terms of stress-displacement in which the maximum tensile stress, equal to 235.3 MPa and corresponding to a maximum load of 29.6 KN, was equal for the two samples. The rupture was always localised at the Al/Fe interface due to the specimen shape.

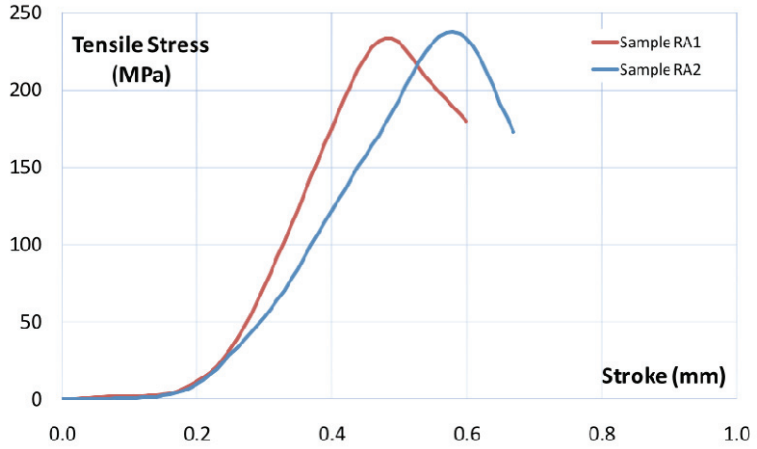

Fig. 28. Tensile stress vs. punch stroke – Samples RA1 and RA2.

Specimen ID	Condition	Al/Fe thick mm/mm	Diameter α (mm)	Tensile T (KN)	Tensile σ (MPa)
-- /RA1-RA2	As-clad	11.0/13.0	12.7	29.6	235.3
LPBAL1 / RB1-RB2	Welded from aluminium side	8.0/10.0	9.7	28.5	226.4
LPBAL2 / RC1-RC2		6.5/10.0	8.2	26.8	213.0
LPBAL3 / RD1-RD2		5.0/10.0	6.7	23.9	199.9
LPBST1 / RE1-RE2	Welded from steel side	11.0/8.5	12.7	28.1	223.7
LPBST2 / RF1-RF2		11.0/7.0	12.7	26.6	211.2
LPBST3 / RG1-RG2		11.0/5.5	12.7	26.1	206.8

Table 16. Ram tensile test – Sample dimensions & results.

Table 16 reports the final results of all tests in term of maximum tensile load and stress. The results showed the same trend detected during the shear test linked to the more evident reduction of the final strength of specimens welded from the aluminium side than those welded from the steel side. The reduction of the distance between the fused area and bond interface was less important because specimens were realised in area far from the laser beam interaction and consequently they were subjected to mild laser-induced thermal loads.
The comparison between mechanical results and inter-metallic film thickness was very interesting. The reduction of the maximum tensile and shear stresses could be inputted to the increase of the inter-metallic film thickness. In fact lower values of the mechanical strength was detected for higher values of the film thickness. This hypothesis also confirmed that specimen welded from the steel side were more critical than those welded from the aluminium side. However, the mechanical strength of the welded specimens were only blindly affected by the laser beam interaction because the measured strengths were much more higher than those normally required.

10. Mechanical strength of laser welded T-joints

Double square fillet (2F) T-joint welds of AA5083 aluminium alloy and ASTMA516 steel base materials were then produced using different welding methods (laser welding with

filler wire and hybrid laser-MIG welding). T-joint welds were realised by joining two 6.0 mm thick plates. Steel (aluminium) 2SF T-joints were produced with the laser beam power equal to 5.5 (5.5) kW in continuous wave regime, travel speed set to 1.9 (1.5) m/min, filler feed equal to 0.8 (1.5) m/min. Additional process parameters kept constant during all tests were the focal length, beam focus position and Helium shielding gas flow-rate, the values of which were 300.0 mm, 0.0 mm (on the surface) and 30.0 Nl/min respectively. The laser head was angled of 51° degree respect to the Z axis to guarantee joint accessibility. The 1.2 mm diameter filler wire was used. The process parameters of the pulsed arc MIG welding during hybrid welding for steel (aluminium) were open arc voltage, peak current intensity, peak time, pulse frequency and background current intensity equal to 40 (27.8) V, 350 (380) A, 2.1 (1.7) ms, 276 (176) Hz, 80 (60) A respectively. The process evaluation in this phase was manly based on weld cross-section shape. Welds with incomplete penetration and high porosity were discarded. Figure 29 reports weld cross sections achieved during experiments. It was decide to considered anymore the hybrid welding process because of excessive undercuts detected.

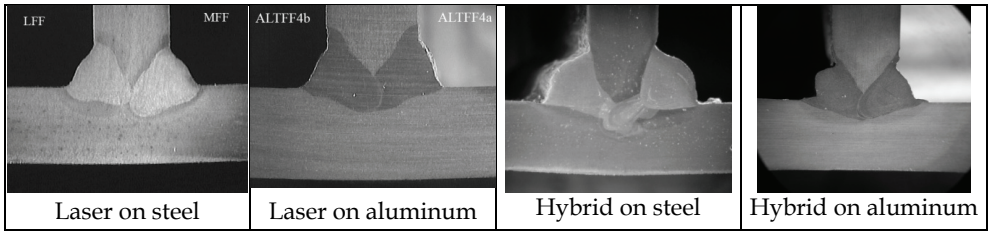

Fig. 29. 2F T-joints.

In the second experimental phase, double side/double square fillet (2S/2F) T-joints of STJ bars were realised, setting-up process parameters previously identified. The main objective was the coupling of the information of bead-on-plate with those coming from 2SF T-joints. In this way, it was possible to evaluate the effects of laser welding on the final joint geometry. Laser welding with filler wire was the only process employed and two classes of specimens were considered. In particular, the STJ were welded in as-clad condition (original height of 25.4 mm) or in condition (final height of 12.0 mm). The machined condition required that thickness of steel and aluminium alloys was reduced to 6.0 mm each by machining. Two 6.0 mm thick web plates were finally joined to STJs. Morphological and metallographic analyses were initially carried out to compare welding techniques and estimate the influence of the heat input on the Al/Fe interface. Figure 30 shows the cross sections of results of this experimental activity for hybrid and laser welding. The results were very similar to those achieved for 2F T-joints. More important was the material testing of 2S/2F T-joints. Specimen cut from centre of each joint were subject to tensile test to assess the mechanical strength (Figure 31). Length of the entire joint and of each specimen were 260.0 and 60.0 mm, according to specifications of American Bureau of Shipping.

Fig. 30. Double side/double square fillet square T-joints.

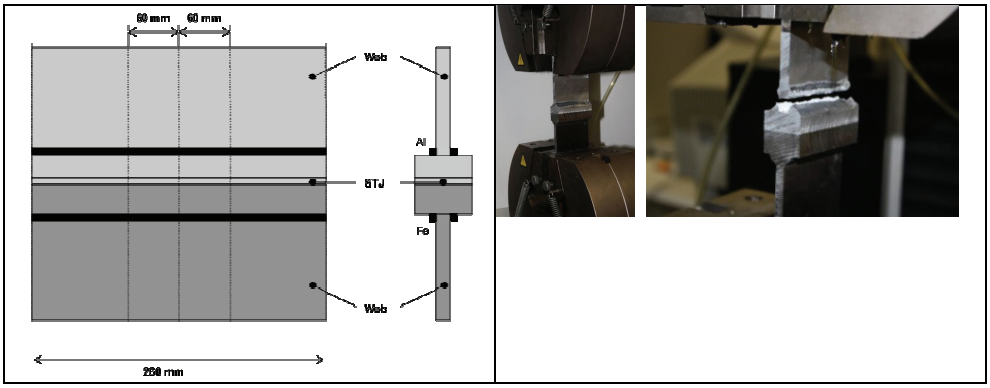

Fig. 31. Tensile test (specimen and equipment).

Tensile test were performed by grabbing both webs along the entire length and moving the crosshead of INSTRON 4485 tensile machine with a travel speed equal to 3.0 mm/min. The tensile test were stop once rupture occurred in web/STJ welds or in aluminium/steel STJ interface. Several tests were performed with several repetitions. The analysis of the results was mainly focused on mechanical strength of 2S/2F T-joints. Table 3 reports the average value between repetitions of the peak tensile load, peak tensile strength and peak tensile load on AA5083 alloy. The first two data were evaluated at bond interface while the last data was calculated at web section for the ultimate tensile strength of AA5083 alloy equal to 300 MPa. Laser beam welding led to joints with god strength in both as-clad and machined condition. All ruptures thus occurred on the aluminium side in aluminium welds or webs, satisfying the strict conditions of MILL-J-24445A (*AAVV, 1997*) for successful testing. According to this standard, each specimen tested must comply with one the following conditions for acceptance: i) failure in one of the web member and ii) failure of the bond surface at a load above that calculated to cause failure in one of the web members, based on the specific minimum tensile strength of the web material. It is possible to note these joints were also able to successfully overcome the second condition of the MIL-J-24445A, with T_{MAX} equal to 155.70 and 148.05 KN, in the hypothesis that rupture was localised in the aluminium/steel interface.

Specimen ID	Condition	Process	Tensile		Tensile	MIL-J-2445A
			T_{MAX} (KN)	σ_{MAX} (MPA)	T_{AA5083} (KN)	
2S/2F1	As-clad	Laser & Filler	155.70	93.04	108.00	YES
Machined	2S/2F2	Laser & filler	148.05	88.47	108.00	YES

Table 17. Tensile test– Sample dimensions & results.

Figure 32 shows the aspect of the rupture surfaces, organised in class of welding according to as-clad or machined state. Laser welded 2S/SF T-joints were characterised from the rupture surface positioned in the aluminium web material with no damage in the weld. The joints in the as-clad condition presented a sound weld. No particular effects were detected. Photos of Figure 33 are the most critic conditions in order to point out some specific outlines discovered during experimentation. The photo at left side represents a specimen in the machined state with aluminium alloy thickness equal to 6.0 mm. In the right side photo thickness of the specimen was further reduced before welding. In this case, the rupture occurred in the aluminium/steel interface and not in the aluminium web, pointing out that heat induced by laser beam welding seriously affected joint integrity if reduction was too high.

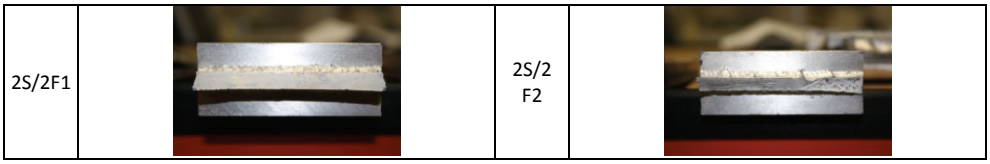

Fig. 32. 2S/2F STJs after rupture (aluminium side).

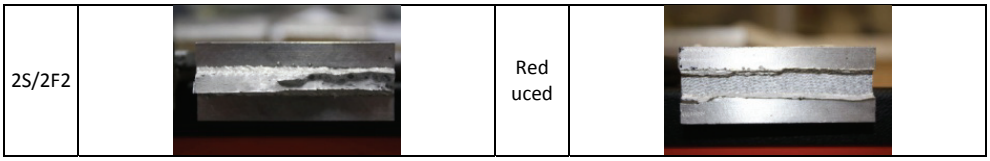

Fig. 33. 2S/2F STJs after rupture in machined state (aluminium side).

In this work the influence of different thermal loads caused by laser beam on mechanical strength of the Fe/Al explosion welded joints has been investigated. The present research has investigated the application of laser beam to weld components made of structural transition joints (STJs) between steel and aluminium base materials. The metallographic examinations and the tensile tests have pointed-out that laser-induced thermal loads strongly promoted inter-metallic growth at aluminium/steel interface. The condition has been also verified by reducing the thickness of the STJ. However, these loads have limited influence on integrity of bead-on-plate welds and double side/double square fillet T-joints because rupture mainly occurred in the web connecting the weakest material (aluminium alloy) with STJ. The condition has been also verified by reducing the thickness of the STJ.

Acknowledgement

The present research is only a part of activities performed by CALEF Consortium (http://www.consorziocalef.it/), the main members of which are the CRF, ENEA, Polytechnic of Bari and Rodriquez Cantieri Navali SPA. In particular, Rodriguez Cantieri Navali SPA directly funded the present research through the ENVIROALISWATH project. The authors wish to thank Dr. Donato SORGENTE and Dr. Gianfranco PALUMBO for their support during experimentation, Dr Marco BRANDIZZI of FIAT Research Center for his suggestions, Dr. Marco VITTORI ANTISARI and Dr. Giuseppe BARBIERI of ENEA –

Casaccia Research Center, Laura CAPODIECI of ENEA – Dept. FIM – Composites & Nanostructured materials Section, Enzo PUTIGNANO and Roberto DEBONIS of CALEF Consortium.

11. References

AAVV, (2000). *American Bureau of Shipping, Materials and Welding*, Supplementary Requirements for Naval Vessels, Part 2 Chapter 11, Section 6, Aluminum/Steel Bimetallic Transition Joints.

AAVV, (2007) *ASM Handbook Volume 6*, Welding, Brazing, and Soldering, Fundamentals of explosion welding.

AAVV, 1997, MIL-J-24445A, Joint, bimetallic bonded, aluminum to steel, Military Specifications and Standards, 25-Jul-1977.

Acarer M., Gülenç B. & Findik F., (2004). The influence of some factors on steel/steel bonding quality on there characteristics of explosive welding joints, *J. of Materials Science*, 39 , 6457-6466.

Bankers J.G., Nobili A., (2002) Aluminium-Steel Electric Transition Joints - Effects of Temperature and Time upon Mechanical Properties, *TMS 131st Annual Meeting*, Seattle (USA), February 17-21, 2002.

Borrisutthekul R. & alii, (2007). Suppression of intermetallic reaction layer formation by controlling heat flow in dissimilar joining of steel and aluminum alloy, *Materials Science and Engineering A*, 467, 108-113.

Bruckner J., Considering thermal processes for dissimilar metals - Joining steel to aluminium in heat-intensive applications, *The Fabricator*, August 28, 2003, http://www.thefabricator.com/Metallurgy/ Metallurgy_Article.cfm?ID=676.

Capodiceci L., (2007). Analysis of Explosion welding steel /aluminum transition joint with Scanning Electronic Microscope and X-Ray Microanalysis, *ENEA Internal Technical Report*, RT/ENEA/06/11 of FIM COMP Dept.

Chao R.M., Yang J.M. & Lay S.R., (1997). Interfacial toughness for the shipboard aluminium/steel structural transition joint, *Marine Structures*, 353-362.

Chen C.M., Kovacevic R., (2004). Joining of Al 6061 alloy to AISI 1018 steel by combined effects of fusion and solid state welding, *Int. J. of Machine Tools & Manufacture*, 44, 1205–1214.

Chen L. & alii, Clad metals, roll bonding and their applications for SOFC interconnects, *Journal of Power Sources*, 152, 40–45.

Deqing W., Ziyuan S. & Ruobin Q., (2007). Cladding of stainless steel on aluminium and carbon steel by interlayer diffusion bonding, *Scripta Materialia*, 56, 369–372.

Durgutlu A., Gulenc B. & Findik F., (2005). Examination of copper/stainless steel joints formed by explosive welding, *Materials and Design*, 497–507.

Kobayashi S. & Yakou T., (2002). Control of intermetallic compound layers at interface between steel and aluminum by diffusion-treatment, *Materials Science and Engineering A*, 338, 44-53.

Jindal V., Srivastava V.C., (2008), Growth of intermetallic layer at roll bonded IF-steel/aluminum interface, *J. of Materials Processing Technology*, 195, 88–93.

Lee J.E. et alii, (2007). Effects of annealing on the mechanical and interface properties of stainless steel/aluminum/copper clad-metal sheets, *J. of Materials Processing Technology*, 187–188, 546–549.

Li S.-X. et al., (2008). Fatigue damage of stainless steel diffusion-bonded joints, *Materials Science and Engineering A*, 480, 125-129.

Missori S., Murdolo F. & Sili A., (2004), Single-Pass Laser Beam Welding of Clad Steel Plate, *Welding Journal*, 02, 65-71.

Montgomery D.C., 2000, *Design and Analysis of Experiments,* 5th Ed., J.Wiley and sons, 1 (2000) 274-275.

Mousavi S.A.A.A., Al-Hassani S.T.S. & Atkins A.G., (2008). Bond strength of explosively welded specimens, *Materials & Design*, 29 , 1334-1352.

Mousavi S.A.A.A., Barrett L.M. & Al-Hassani S.T.S., (2008). Explosive welding of metal plates, *J. of Materials Processing Technology*, 1-3, 224-239.

Mousavi S.A.A.A. & Sartangi P.F., (2008). Effect of post-weld heat treatment on the interface microstructure of explosively welded titanium–stainless steel composite, *Materials Science and Engineering A*, 494, 329-336.

Naoi D. & Kajihara M., (2007), Growth behavior of Fe_2Al_5 during reactive diffusion between Fe and Al at solid-state temperatures, *Materials Science and Engineering A*, 459, 375-382.

Peyre P. & alii, (2007). Generation of aluminium–steel joints with laser-induced reactive wetting, *Materials Science and Engineering A*, 444, 327-338.

Sierra G. & alii, (2007). Steel to aluminium key-hole laser welding, *Materials Science and Engineering A*, 447, 197-208.

Tricarico L. & alii, (2007). Effects of laser welding on properties of Al/Fe explosionwelded structural transition joints, *ATA Proc. of 2nd Int. Conf. on "Advanced Materials and Technologies for Transportation Industry*, ELASIS in Pomigliano D'Arco (Italy), October 18-19 2007.

Young G.A., Banker J.G., Explosion Welded, Bi-Metallic Solutions to Dissimilar Metal Joining, *13th Offshore Symposium*, February 24, 2004, Houston (USA).

Watanabe T., Takayama H., Yanagisawa A. (2006). Joining of aluminium alloy to steel by friction stir welding, *Journal of Materials Processing Technology*, 178, 342–349.

Vollertsen F. (2005). Developments and trends in laser welding of sheet metal, *Advanced Materials Research*, 6-8,59-70.